Research Article Vol. 31, No. 3 / 30 Jan 2023 / Optics Express 3998
Optics EXPRESS

Upgraded Cherenkov time-of-flight detector for the AFP project

LIBOR NOZKA,[1,*] GIULIO AVONI,[2] ELZBIETA BANAS,[3] ANDREW BRANDT,[4] KAREL CERNY,[1] PAUL M. DAVIS,[5] SERGE DUARTE PINTO,[6] VJACESLAV GEORGIEV,[7] MIROSLAV HRABOVSKY,[1] TOMAS KOMAREK,[1] KRZYSZTOF KORCYL,[3] IVAN LOPEZ-PAZ,[8] MARKO MILOVANOVIC,[9] GORAN MLADENOVIC,[10] DMITRY A. ORLOV,[6] MICHAEL RIJSSENBEEK,[11] PETR SCHOVANEK,[12] TOMAS SYKORA,[13] MACIEJ TRZEBINSKI,[3] VLADIMIR URBASEK,[12] AND JAN ZICH[7]

[1] *Joint Laboratory of Optics of Palacky University and Institute of Physics AS CR, Faculty of Science, Palacký University, 17. listopadu 12, 771 46 Olomouc, Czech Republic*
[2] *INFN Bologna and Universita di Bologna, Dipartimento di Fisica, viale C. Berti Pichat, 6/2, IT – 40127 Bologna, Italy*
[3] *Institute of Nuclear Physics Polish Academy of Sciences, Cracow, Poland*
[4] *The University of Texas at Arlington, Department of Physics, Box 19059, Arlington, TX 76019, USA*
[5] *Centre for Particle Physics, Department of Physics, University of Alberta, Edmonton, AB T6G 2G7, Canada*
[6] *Photonis Defense Inc., 1000 New Holland Ave., Lancaster, PA 17601, USA*
[7] *University of West Bohemia, Dept. of Applied Electronics and Telecommunications, Univerzitni 26, Pilsen, 30100, Czech Republic*
[8] *Institut de Física d'Altes Energies (IFAE), The Barcelona Institute of Science and Technology (BIST), Campus UAB, 08193 Bellaterra (Barcelona), Spain*
[9] *DESY, Platanenallee 6 D-15738 Zeuthen, Germany*
[10] *University of Belgrade - Faculty of Mechanical Engineering, Kraljice Marije 16, Belgrade, Serbia*
[11] *Stony Brook University, Dept. of Physics and Astronomy, Nicolls Road, Stony Brook, NY 11794-3800, USA*
[12] *Institute of Physics of the Academy of Sciences of the Czech Republic, Na Slovance 2, Prague, Czech Republic*
[13] *Charles University, Faculty of Mathematics and Physics, Institute of Particle and Nuclear Physics, V Holesovickach 2, CZ - 18000 Praha 8, Czech Republic*
[*] *libor.nozka@upol.cz*

Abstract: We present the results of our performance studies of the upgraded Cherenkov time-of-flight (ToF) detector for the AFP (ATLAS Forward Proton) project. The latest version consists of solid L-shaped fused silica bars, new customized ALD-coated micro-channel plate photomultipliers (MCP-PMTs) miniPlanacon XPM85112-S-R2D2 with an extended lifetime which operate at low gains (order of 10^3), and an updated construction. The improvements were aimed to increase the efficiency, the lifetime as well as the radiation hardness of the detector which has been designed to operate in high radiation areas (above 400 kGy/year). The detector was finally tested at the CERN-SPS test-beam facility (120 GeV π^+ particles) in August 2021 prior to its installation at the Large Hadron Collider (LHC) at CERN. Measurements proved the detector kept its inner timing resolution of 20 ps despite the rather low gain of its photodetector and reduced optical throughput caused by inevitable changes in the detector geometry.

#480624 https://doi.org/10.1364/OE.480624
Journal © 2023 Received 11 Nov 2022; revised 16 Dec 2022; accepted 27 Dec 2022; published 19 Jan 2023

Optics EXPRESS

1. Introduction

The design and the physics motivation needed for the time-of-flight (ToF) subdetector for the ATLAS-AFP project itself has already been described thoroughly in our previous papers: the physics concept in [1–3] performance studies in [4]; simulation benchmark studies in [5]; details of the optics in [6]; and timing studies in [6,7]. The ToF detector has been designed as a part of the proton tagging detector AFP to decrease the background to central exclusive production processes $p + p \rightarrow p + X + p$ where X stands for the centrally produced system, which could consist of a pair of jets, a pair of intermediate vector bosons (W^+W^-), or a Higgs boson H. It operates at high radiation levels above 400 kGy/year or $4 \cdot 10^{15}$ n_{eq}/cm^2 (the n_{eq} stands for a neutron equivalent dose of an energy of 1 MeV) at 5 mm from the beam centre.

For clarity, the geometry of the ToF detector is depicted in Fig. 1. The ToF assemblage consists of a 4×4 matrix of L-shaped bars made of fused silica (SK-1300 by O'Hara, optical constants in [5]). The outer dimensions of the matrix are a height of 73.3 mm, a width of 65.5 mm (in the direction of radiators), and a depth of 25.2 mm. The dimensions of each bar are reported in [6]. Each bar serves both as a Cherenkov radiator and a light guide towards a fast multichannel-plate photomultiplier (MCP-PMT) device (the sensor plane in Fig. 1). There is a thin mirror optical layer on the 45° cut surface in the bar elbow.

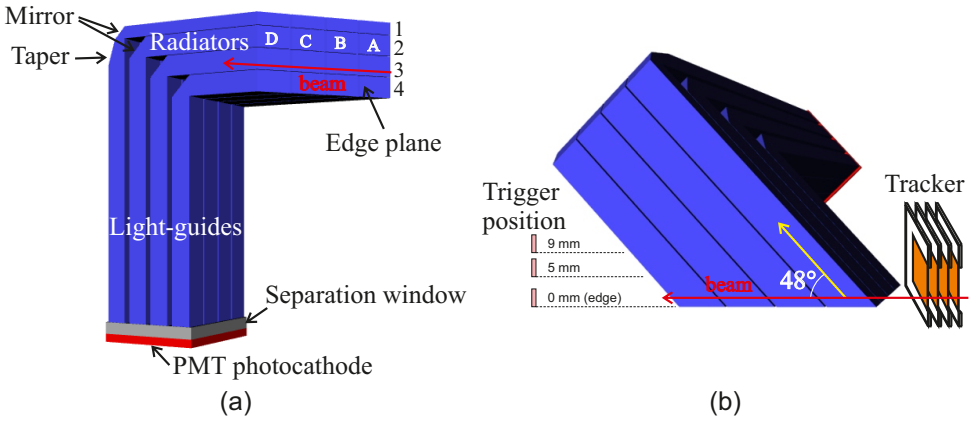

Fig. 1. Optical part of the ToF subdetector made for test measurements: (a) side view with (b) top view together with position of the tracker and three positions of the SiPM trigger used during test measurements. The trigger position is measured relatively to the edge plane which is common for all the bars.

Besides this, the bars of the Train 1 are equipped with an extra polished surface, called taper, to further enhance their optical throughput [5]. The rows of four bars along the beam direction are called trains and are labeled with a number. The bars in each train are labeled with the letters A, B, C, and D along the direction of the incoming particles. In this way, the bars in the Train 1 are labeled 1A, 1B, 1C, and 1D and so on for the other trains. The acceptance area of the AFP detector is 16.8×20.0 mm^2, given by the dimensions of a tracker module at the front [8] and its tilt as illustrated in the Fig. 1. In the past, L-shaped bars were constructed so that the two arms of a bar were produced separately and then glued together [6]. For the ToF upgrade, we decided to make the bars solid (without glue) which made the production more complex. The glue-free solution improved the optical throughput of the optical system by 18%, see also Fig. 4 in [6], and the radiation hardness [9].

In our previous design, both the optics (bars) and the photomultiplier were placed inside the Roman Pot which was evacuated to a rotary vacuum (5-50 mbar). It was necessary to treat the photomultiplier and its high-voltage cables in a special way to avoid any accidental discharge

Optics EXPRESS

spikes (we operated at the bottom part of the Paschen curve here). To remove this problem, the upgraded ToF detector introduced a separation of the photomultiplier from the vacuum side, see Fig. 2. The evacuated area is inside a Roman Pot covered by a detector flange on its open side. Both ToF and tracker detectors are installed here, except for the ToF's photomultiplier which is inserted in a movable tube going through a hole in the detector's flange. A 2.9 mm thick window separates the photomultiplier from the vacuum side. The window is made of the same material as bars (fused silica, SK-1300). It was coded by a simple anti-reflection layer made of 35 nm thick MgF_2 and annealed at 300°C. It is an additional optical element on the Cherenkov pulse path towards the photodetector resulting in a decrease of the total throughput of the ToF optics. The movable tube allows for the easy and precise alignment of the whole ToF detector with respect to the tracker thanks to a set of four precision screws mounted in the far end of the tube, see Fig. 2. The vacuum tightness around the tube is achieved by means of a custom-made bellows (by Mewasa AG, Switzerland).

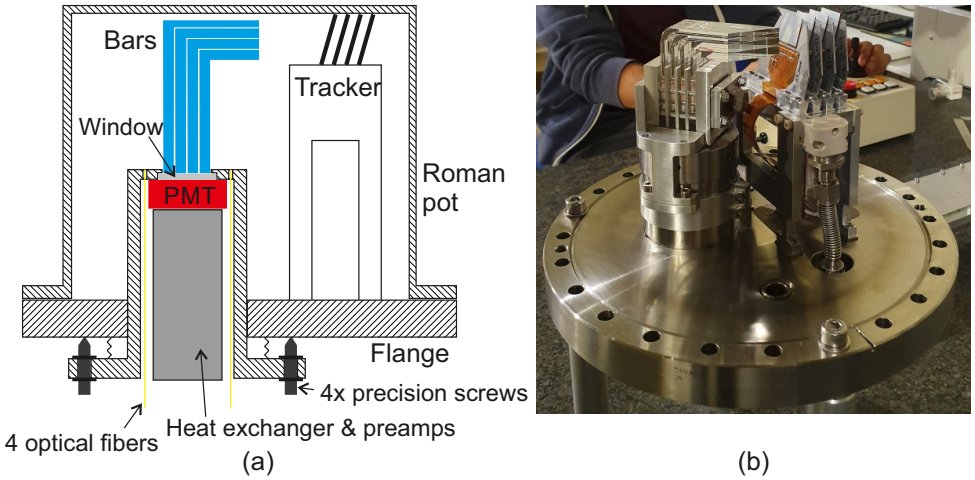

Fig. 2. AFP detector with the upgraded ToF detector: (a) schematic view inside the Roman pot – area inside the Roman pot is evacuated, (b) real view on the assembly (without the pot).

Photonis produced four new photomultipliers miniPlanacon XPM85112-S-R2D2 for us: S/N 9002196 (labelled as #2196, MCP resistance 44 MΩ); 9002199 (#2199, 35 MΩ); 9002200 (#2200, 27 MΩ); and 9002201(#2201, 55 MΩ). They have a fused silica entrance window and a Bialkali photocathode. Their two-stage multi-channel plate (MCP) was ALD-coated (resistive and secondary emissive layers) by Arradiance to achieve an extended lifetime above 10 C/cm^2. The PMTs #2196 and #2199 have a standard anode gap of 2.9 mm. The PMTs #2200 and #2201 have a reduced anode gap of 0.6 mm. The backend electronic circuits of all photomultipliers were redesigned to reduce electronic crosstalk between anode pads (pixels) and to adapt to the new preamplifiers of the first stage [10]. Like the original design by Photonis, the back-end electronics were realized by two printed circuit boards (PCBs): the bias PCB and the anode PCB, each with a size of 32×32 mm^2, see Figs. 3(a) and 3(b). In the bias PCB, the original MCP-OUT bias resistor was removed because it caused crosstalk between the anode pads and it had no meaning for separate readouts of pixels. We also optimized wires lengths to make the same propagations delays among the channels. We enlarged auxiliary connecting Nickel strips to reduce parasitic impedances as well. The default output pinout on the anode PCB (pin header) was replaced by an equally spaced grid of 50 Ω RF MMCX female connectors, Fig. 3(c), to connect the new coaxial one-channel preamplifiers PA-a, Fig. 3(d). Having lower MCP resistance, the PMTs #2199 and #2200 were candidates for installation to the ToF and here we report mostly on the results of

Optics EXPRESS

using these devices. The #2196 was used as a backup and for future test measurements. The #2201 PMT was considered for radiation hardness tests.

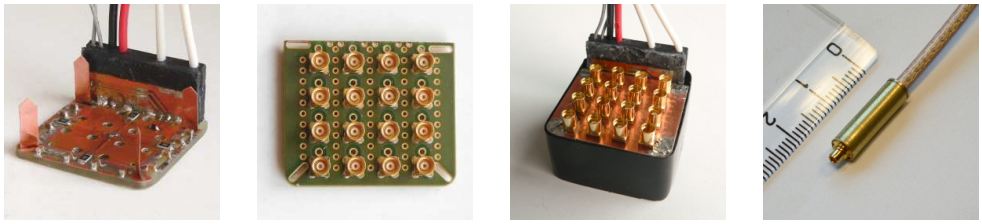

Fig. 3. Snapshots from the construction of a prototype of the modified version of the photomultiplier XPM85112: (a) the bias PCB equipped with a black HV input block and four Nickel strips for grounding connection with the anode PCB; (b) the anode PCB with MMCX female connectors; (c) assembled prototype with both PCBs; (d) coaxial one-channel preamplifier stage with MMCX connectors (Pa-a).

The PA-a preamplifiers are current-to-voltage converters with the conversion constant of 25 mV/mA and a voltage amplification of 20 dB (10×). They are equipped with MMCX male connectors on the PMT side and a 1.7 m long coaxial cable with the same MMCX ending on the other side. This solution ensures better protection against outside electromagnetic interference, an easier replacement of a damaged PA-a, and improved heat removal through the body of the detector. The PA-as are supplied from next voltage-to-voltage preamplifiers - PA-b modules. PA-bs are in the form of NIM modules. Each NIM module consists of a control motherboard and eight one-channel daughter boards with two stages of voltage-to-voltage preamplifiers with the total gain of 39 dB with available attenuation by 31.5 dB. Note that the gain varies among individual channels with an uncertainty range of ±1dB (±10%). Each channel is provided with a low-pass analog filter with a cut-off frequency of 1.4 GHz for noise rejection (LFCG-1400+ by Mini-Circuits).

This latest version of the ToF detector was subject to several performance measurements. It is known that the gain of the MCP photomultipliers decreases with increased repetition frequency (rates) of incoming light pulses [11] depending on the initial gain (at low kHz rates). We plan to use our photomultipliers on the gain of around 2000 based on our preliminary tests (it is ten times less than in our previous ToF detector). We refer to this gain as the DC gain because it was measured by a producer in a so-called DC mode [12]. Such low gain allows us to suppress the negative effect of high rates on the actual gain of the photomultiplier at the cost of a worse timing resolution. As the ToF detector will run in the LHC with an expected event rate of 20 MHz per train, we needed to address the behavior of the photomultipliers at high rates. These rate measurements were done in our laboratory on a setup with a pulsed picosecond laser. The results are reported in [10]. We found out that there was no significant gain deterioration of the PMTs #2199 and #2200 at the rate of 20 MHz and their timing resolution was 23 ps and 16 ps respectively (for 25 photoelectrons). The gain of the #2196 dropped by 42% at a 20 MHz rate and its timing resolution got worse: from 23 ps to 40 ps.

The timing performance of the whole ToF detector was the goal of the measurements made at the CERN-SPS test-beam facility (120 GeV π^+ particles) in August 2021 prior to its installation at the Large Hadron Collider (LHC) at CERN. Our first measurements with solid (glue-free) bars were performed in 2019 in DESY (Hamburg, Germany) in an electron beam with the energy of 5 GeV [9]. But the characteristics of such a beam are rather different from that of an LHC proton beam. We therefore focused on measurements with the 120 GeV π^+ beam which had very

Optics EXPRESS

similar effects on our detector as the LHC proton beam (mainly a high production of secondary particles on the DESY beam).

2. Simulation studies

The overall optical throughput of the upgraded ToF optical part changed if compared to the previous version. Removing the glue from the bars resulted in an increase of their optical throughput by at least 23% due to an additional increase of the wavelength region from 165 to 235 nm [9]. On the other hand, the separation window introduces extra losses due to its attenuation and the additional two optical interfaces of glass-air (authors are not aware of an optical grease suitable at high radiation levels of 400 kGy or more). The performance predictions of the new optics on the SPS beam were simulated in the Geant4 simulation framework [13]. The transverse geometrical profile of the passing pion beam was a square 3×3 mm^2 (particle positions randomly scattered in it) to mimic the acceptance window given by the size of the trigger used in the beam test measurements, see Fig. 1(b) and the next section. The ToF model embodies all optical parts and a model of the photocathode of the photomultiplier using experimental values of its quantum efficiency (QE) [14]. The spectral range of Cherenkov light was restricted to the range from 160 nm to 650 nm. The lower limit was due to the absorption edge of the glass SK-1300 and the upper limit due to a low QE of the photocathode above 650 nm. As there are no known values of QE below 200 nm, we assigned the value 0.16 at the lowest known wavelength of 200 nm to the region down to 160 nm. The collection efficiency η of the photomultiplier was set to 0.6 (set by producer). A model of the separation window was used in the simulation which included the anti-reflection layers on both sides of the window.

As the measurements were focused on the Train 2, results for the Bar 2A (the first one) and 2D (the last one) were investigated in the simulation studies. Hereafter, when we speak of a bar performance, we mean the whole channel including the bar, the photocathode, and a corresponding pixel of the photomultiplier. The results of the simulation showed that the presence of the separation window decreased the total optical throughput by 16%. This is caused by attenuation in the window itself, but it is mainly due to Fresnel losses at additional air/vacuum-glass optical interfaces.

Regarding the comparison of glued and solid bars, Table 1 summarizes the number of photoelectrons produced on the photomultiplier's photocathode for the glued and the solid bars of the Train 2. The results presented are valid for the trigger position at the edge, 5 mm, and 9 mm from the edge, see Fig. 1(b). The following observations can be made:

- Solid bars benefit from the presence of deep UV photons. For all types of bars (A-D), the solid bars produced more photoelectrons than their glued counterparts by a factor of 1.7-1.8.
- Among solid bars, the Bar 2D produced more photoelectrons than 2A by a factor of 1.2. The multiplication factor was the same among the glued bars.
- Bars A always produced fewer photoelectrons than Bars B, C, and D because the bars upstream the beam receive the part of the Cherenkov light leaking from the downstream bars [7]. However, this effect depends on the distance of the passing particle from the edge. It is pronounced for large distances from the edge as seen on ratios 2X/2A in the table.

Note the relatively high standard deviations which correspond to the low number of photoelectrons with high fluctuations produced in general. The Cherenkov pulse is generated within 27 ps by a passing relativistic pion in a bar (or proton in the case the LHC). The pulse stretches out on its way to the photocathode due to the geometry of the bar and a significant dispersion of its refractive index in the ultraviolet region. Figure 4(a) shows how wavelengths of incoming photons are distributed in time on the sensor for the solid Bar 2D (but relevant for all solid bars

Optics EXPRESS

without glue). The pulse length is 500 ps in the case of the solid bars. The glued bars suppress the light below 235 nm resulting in the final pulse length of 250 ps. The time distribution of produced photoelectrons on a photocathode is in Fig. 4(b) where photoelectrons are counted in 25 ps wide time slices. A small spread of produced photoelectrons in time results in a better shape of the falling edge and a higher amplitude (in absolute value) of the output signal from the photomultiplier. This has a positive impact on the timing performance in general. From this point of view, the light dispersion in bars affects the timing resolution rather negatively. It is assumed that the falling edge of the signal is mostly formed by photoelectrons produced in the first 250-300 ps. From this point of view, photons from the low ultraviolet end of the wavelength spectra do not contribute to the final timing performance of the detector. In the first 300 ps however, the solid bars still produce 1.7 times more photoelectrons than their glued counterparts.

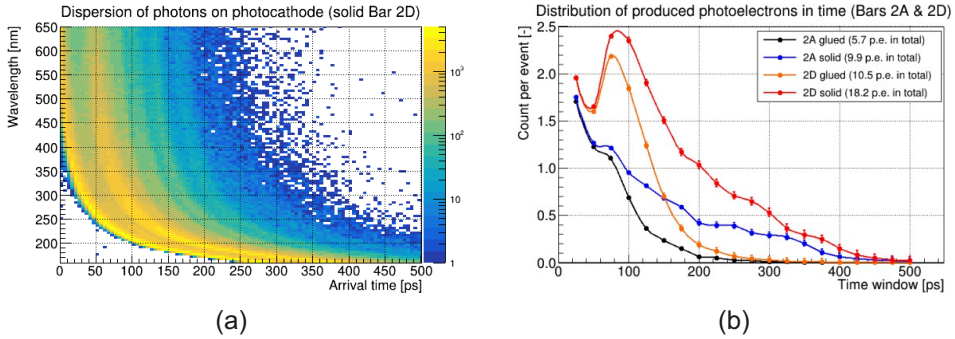

Fig. 4. (a) Simulated time dispersion of the Cherenkov pulse for the solid Bar 2D, and (b) time spread of produced photoelectrons in the Bars 2A and 2D, solid and glued, calculated in 25 ps wide time slices (results valid for the beam π^+ 120 GeV, QE in [14], η=0.6, presence of the separation window, and trigger position at 5 mm from the edge).

Table 1. Number of photoelectrons produced in the Train 2 with glued or solid bars. The parameter S/G stands for the ratio solid/glued of number of photoelectrons (results valid for the beam π^+ 120 GeV, QE in [14], η=0.6, and installed separation window).

	Edge			5 mm			9 mm		
Bar	Glued	Solid	S/G	Glued	Solid	S/G	Glued	Solid	S/G
2A	9 ± 3	16 ± 4	1.8 ± 0.7	6 ± 2	10 ± 3	1.7 ± 0.7	6 ± 2	10 ± 3	1.7 ± 0.7
2B	11 ± 3	19 ± 4	1.7 ± 0.6	9 ± 3	15 ± 4	1.7 ± 0.7	6 ± 2	10 ± 3	1.7 ± 0.7
2C	11 ± 3	19 ± 4	1.7 ± 0.6	10 ± 3	18 ± 4	1.8 ± 0.7	9 ± 3	16 ± 4	1.8 ± 0.7
2D	11 ± 3	19 ± 4	1.7 ± 0.6	10 ± 3	18 ± 4	1.8 ± 0.7	10 ± 3	17 ± 4	1.7 ± 0.6
ratios									
2B/2A	1.2 ± 0.5	1.2 ± 0.4		1.5 ± 0.7	1.5 ± 0.6		1.0 ± 0.5	1.0 ± 0.4	
2C/2A	1.2 ± 0.5	1.2 ± 0.4		1.7 ± 0.7	1.8 ± 0.7		1.5 ± 0.7	1.6 ± 0.6	
2D/2A	1.2 ± 0.5	1.2 ± 0.4		1.7 ± 0.7	1.8 ± 0.7		1.7 ± 0.7	1.7 ± 0.6	

Estimation of the signal characteristics Photoelectrons produced in the PMT's photocathode and accepted in the first multi-channel plate (MCP) are then multiplied in both multichannel plates of the PMT. As mentioned above, the DC gain G of the PMT embodies its collection efficiency of η. For simulation purposes, one needs to use a gain valid for a single-photoelectron input which is not affected by η. Here, it is called the single-photoelectron gain G_{SPE} (it is labeled as G_{PHD} in [12]). Roughly, $G \cong \eta G_{SPE}$ where $\eta \approx 0.6$ (given by the producer). All used

Optics EXPRESS

photomultipliers (#2196, #2199, and #2200) were operated on the high voltage of 1545 V. The G values of the photomultipliers were: 1800 (#2196), 2300 (#2199), and 2100 (#2200) with an uncertainty range of ±15%. The charge generated at the MCP output is then drained away through the backend electronics of the PMT and is then measured as a voltage drop on an anode resistor in the first amplification stage. The preamplifier thus serves as a current-to-voltage (A/V) converter. An equivalent electrical circuit of our photomultipliers is shown in Fig. 5 together with the input part of the first stage amplifier (PA-a). It includes impedances of real components as well as parasitic impedances (in gray). The frequency response (transfer function) of this description is shown in Fig. 6(a). The circuit acts as a low-pass filter with a cut-off frequency of 2.2 GHz (#2200 with a reduced anode gap of 0.6 mm) or 2.5 GHz (#2196 and #2199 with a regular anode gap of 2.9 mm). The current-to-voltage conversion is realized by the 50 Ω anode resistor R_a. However, its parallel wiring to the input impedance Z_i (50 Ω) of the preamplifier represents a total load impedance Z_L of 25 Ω. The input impedance Z_i of the PA-a preamplifier depends on the frequency. Its precise estimation for frequency content of our typical signal shape is outside the scope of this paper. Here, its mean value is expected to lie in an uncertainty range of ±5% around its nominal value.

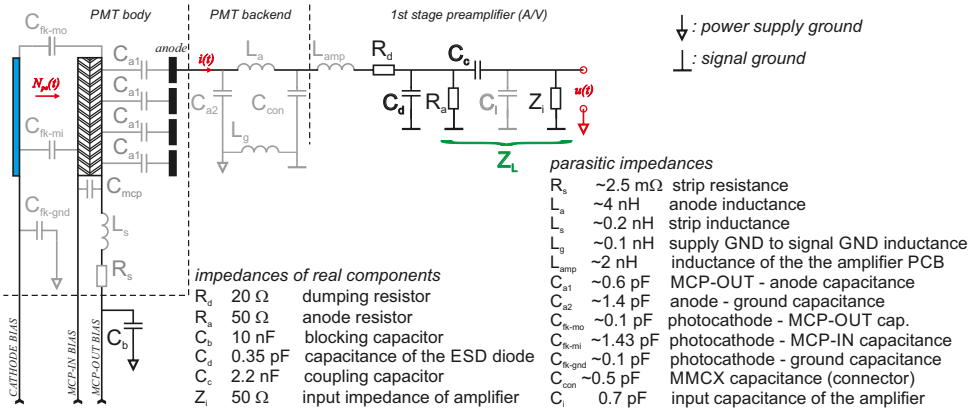

Fig. 5. Equivalent electrical circuit of the miniPlanacon XPM85112-S-R2D2 (one channel) designed by our group and implemented by the producer Photonis, together with the input part of the first-stage preamplifier (parasitic impedances in gray color). Z_L is the total load impedance.

The values of the parasitic impedances were estimated by direct calculations based on the corresponding geometrical and material specifications. Those of them having reductions measurable on the signal strength are listed in Table 2 with their (estimated) nominal value, range of realistically possible values, and effects on the signal shape. The rest of the parasitic impedances in the model have a negligible effect on the resulting amplitude as they are not directly part of the signal path. Note the parasitic anode inductance L_a has a positive effect on the signal amplitude at the expense of the steepness of the pulse. This is because its higher values shift the cut-off frequency of the back-end electronics towards lower frequencies. The strip inductance L_s affects the crosstalk among the pixels. Its higher value increases the strength of the signal on the common MCP-OUT wire causing higher crosstalk. The crosstalk signal behaves opposite the pulse causing a distortion of the pulse edge when added to a proper signal pulse generated at anode pads.

Using this model in the LtSPICE [15] simulation toolkit, the goal was to estimate a signal shape at the impedance load Z_L produced by a bunch of generated photoelectrons N_{pe} in pulse (pe or p.e. stands for photoelectron(s)). The MCP was simulated as a current source producing

Optics EXPRESS

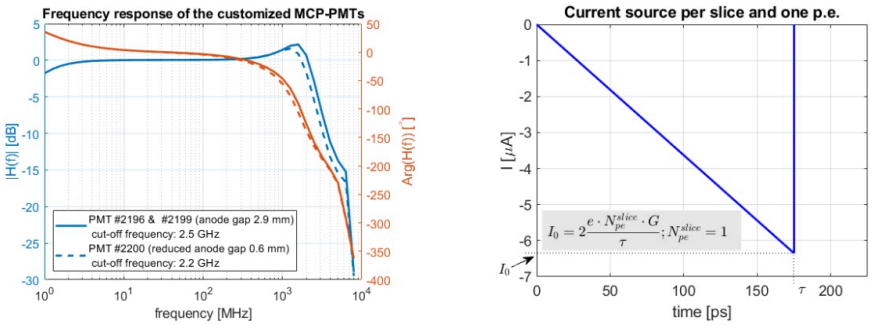

Fig. 6. (a) Frequency response of the customized MCP-PMTs (acting as a low-pass filters), (b) triangular current pulse generated by the MCP from one photoelectron used for calculations of output signal waveforms (example plot valid for PMT #2200).

Table 2. Parasitic impedances, their estimated nominal values, and ranges of possible values (other parasitic impedances in Fig. 5 are taken as known with a nominal value). Correlation (positive) and anti-correlation (negative) effect of an impedance on the amplitude means that its growth causes an increase and decrease of the amplitude (in its absolute value) respectively.

Impedance	Nominal value	Lower limit	Upper limit	Effect on signal amplitude
C_{a1}	0.1 pF (2.9 mm)[a]	–	–	anti-correlates, decrease by 8% when changing from 0.1 to 0.5 pF
	0.5 pF (0.6 mm)[a]	–	–	
C_i	0.7 pF	0.3pF	2.1 pF	anti-correlates, 7%[b]
C_{con}	0.9 pF	0.2 pF	1 pF	anti-correlates, 3%[b]
L_a	2.5 nH	1.5 nH	9.5 nH	correlates, 3%[b]
L_s	0.2 nH	0.05 nH	1.25 nH	correlates, 6%[b]
L_{amp}	2 nH	0.5 nH	3 nH	correlates, 0.3%[b]
L_g	0.1 nH	0.05 nH	1.3 nH	correlates, 1%[b]

[a]Value of C_{a1} depends on the size of the anode gap (2.9 mm for PMTs #2196 and #2199, 0.6 for PMT #2200),
[b]Relative change of the amplitude when changing the impedance from the lower to upper limit.

current impulses in time. Time profiles of the N_{pe} was extracted from the Geant4 simulation for the solid Bar 2D and the glued Bar 2A (the highest number of produced photoelectrons vs. the lowest amount) in the form of 25 ps wide time slices according to the profiles in Fig. 4(b). For each slice in time, a simple current source was proposed generating a triangle pulse according to the shape in Fig. 6(b). The current amplitude I_0 was set to $2eN_{pe}^{slice}G_{SPE}/\tau$ where e is the elementary charge, N_{pe}^{slice} is the number of accepted photoelectrons in a given time slice, G_{SPE} is the single-photoelectron gain of the photomultiplier and τ = 175 ps is the estimated rise time of the current pulse in the MCP [16].

In summary, there was a set of impulse current sources with various strengths defined by a given N_{pe}^{slice} distributed in time according to the time distribution of the photoelectrons produced, as seen in Fig. 7(a) for the PMT #2200. The total current profile was saw-toothed, but the discrete changes lay in the frequency range of tens of GHz and were effectively smeared out by the electronics of the photomultiplier (a low-pass filter as mentioned above). The output signal based on this input is in Fig. 7(b) for both the glued and solid bars geometries.

Optics EXPRESS

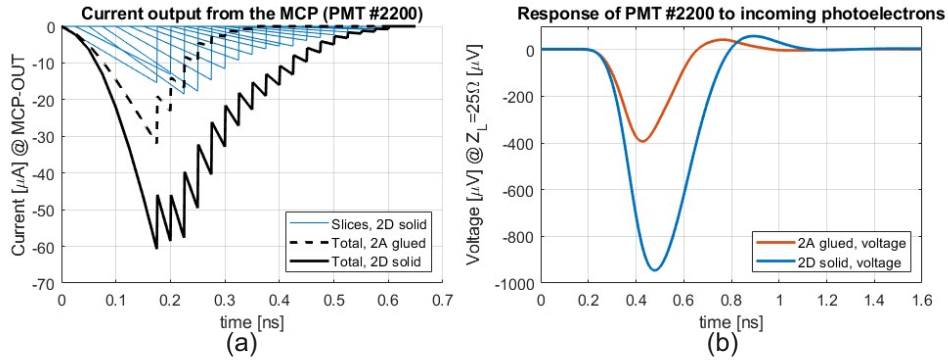

Fig. 7. Simulation of the PMT #2200 response: (a) electric current at the output of the MCP as a sum of contributions by photoelectrons arriving in 25 ps wide time slices for Bars 2A glued and 2D solid at 5 mm from the edge, (b) corresponding output voltage on the total impedance load Z_L.

By definition, the pulse voltage area A_u^L (more precisely the pulse integral) measured at the load resistance is directly related to the generated charge Q:

$$Q = \int_0^\infty i(t) \cdot dt = \frac{1}{Z_L} \int_0^\infty u(t) \cdot dt = \frac{1}{Z_L} A_u^L \tag{1}$$

where $i(t)$ is the current draining the charge through the Z_L and $u(t)$ is the corresponding voltage at the load impedance. The total charge generated on the anode pad is $Q = -eN_{pe}G_{spe}$ where e is the elementary charge, N_{pe} is the number of photoelectrons accepted in the MCP of the photomultiplier, and G_{spe} is the single-photoelectron gain of the MCP. Adding to the Eq. (1), the pulse area is linked to the N_{pe} as follows:

$$A_u^L = -e \cdot G_{SPE} \cdot Z_L \cdot N_{pe} \equiv p \cdot N_{pe} \tag{2}$$

Assuming Z_L constant, the parameter p depends only on the used gain of the photomultiplier. It is in units of [V·s/p.e.] or [Wb/p.e.] (although not intuitive, the unit V·s is actually the unit of magnetic flux Wb (Weber)).

The signal area A_u^L at the load impedance is highly correlated to its amplitude a_u^L through $A_u^L = k_s a_u^L$. The constant k_s is a time constant. It is the width of an equivalent rectangular pulse with the amplitude of the original one and the same charge content. Adding to Eq. (2), we get:

$$a_u^L = \frac{e \cdot Z_L \cdot G_{spe}}{k_s} N_{pe} \equiv k \cdot N_{pe} \tag{3}$$

where k is an amplitude yield per one photoelectron in units of [V/p.e.].

By definition, $p = k_s k$. The k_s is a function of the pulse shape. As the signal is amplified in the amplification chain, the pulse is extended in time in such a way that its amplitude decreases keeping its area constant. Thus consequently, k_s increases. Unless an appropriate backward correction is applied, one should rather focus on the pulse area because this quantity is minimally distorted on the signal pathway.

Table 3 summarizes the calculated values of k_s, k, and p for all used photomultipliers at a given gain. These values were obtained directly from an analysis of the simulated output pulse shapes as discussed above assuming the results presented in Fig. 4(b) and Fig. 7. They are in agreement with Eqs. (1–3) which means the presented mathematical description is consistent with the ltSPICE model.

Optics EXPRESS

Table 3. Parasitic impedances, their estimated nominal values, and ranges of possible values (other parasitic impedances in Fig. 5 are taken as known with a nominal value).

PMT	G [-]	k_s [ps]	k [μV/p.e.]	p [fWb/p.e.]
#2196	1800	232	−43	−10
#2199	2300	232	−55	−13
#2200	2100	252	−45	−12

Note that the values of k_s and k in Table 3 are valid only at the impedance load. The signal pulse is smeared in the amplification chain due to losses in coaxial cables and mostly in the low-pass filter in the PA-b unit. Their values differ from ones calculated from amplified signal characteristics $a_u = g \cdot a_u^L$ and $A_u = g \cdot A_u^L$ (where g is the amplification of the preamplifiers). The smearing affects also the pulse rising edge. In the example shown in Fig. 7(b), the measured value of k_s is 507 ps which is about twice higher than that in the impedance load predicted by the simulation. The p is preserved by definition (Eq. (2)) which is equivalent to the assumption of preserving the pulse area (after dividing by the amplification gain).

3. Experimental setup

The experimental measurements were done on the H6 beamline of the SPS North Area at CERN [17] in the middle of August 2021. The facility provided a π^+ beam of the energy 120 GeV with rates of tens of kHz. The experimental setup was like the one used in our previous measurements in DESY [9]. The only change was to use the Roman pot with the upgraded ToF. The scheme of the measurement setup is shown in Fig. 8 together with a picture of the typical arrangement of the experimental setup.

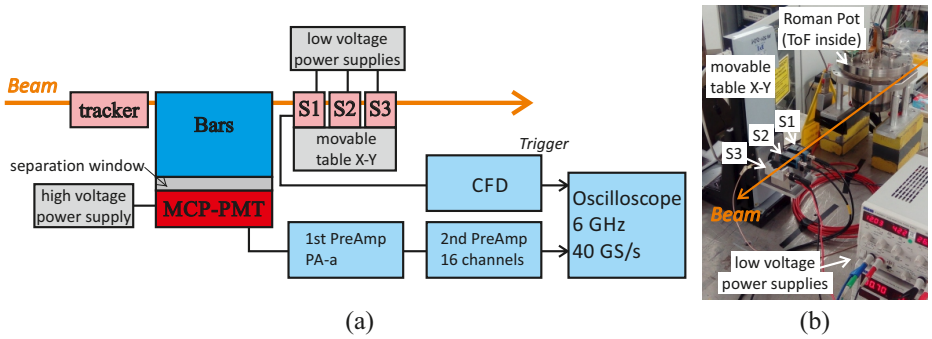

(a) (b)

Fig. 8. (a) Scheme of the experimental setup, (b) typical arrangement of the measurement setup on beam test measurements.

There were used the new MCP photomultipliers #2199, #2196, and #2200 (XPM85112-S-R2D2) by Photonis described above. The photomultipliers were operated at 1545V using a HV divider with a ratio of 1:10:1 (500 kΩ : 5 MΩ : 500 kΩ) providing the gain 1800 (#2196), 2300 (#2199), or 2100 (#2200). The Train 2 with the full complement of 4 bars (solid or glued) was installed on top of the separation window and aligned to its pixelization [6]. The output signal from each pixel (channel) was amplified by the PA-a and PA-b preamplifiers mentioned above providing the total amplification gain of 1000. This value includes the attenuation of the 1.7 m long cable being part of the PA-a amplifier. The amplified signal was collected by means of a fast LeCroy WaveMaster 806Zi-B oscilloscope (bandwidth of 6 GHz, sampling of 40 GS/s).

Optics EXPRESS

The oscilloscope was triggered by the signal from one of three detectors S1, S2, and S3 downstream of the beam. Each trigger detector consisted of a 15 mm long fused silica bar of 3×3 mm^2 cross-section coupled to a silicon photomultiplier (SiPM) manufactured by ST Microelectronics (S1, S2, type: NRD09_1 with 3.5×3.5 mm^2 and 58 μm cell size) [18,19] or by SensL (S3) [20] that detected Cherenkov radiation. They were placed on a two-axis movable stage (remotely controlled) in the beam-transverse plane to select a specific area of the ToF detector for study. The first detector S1 (the closest to the ToF) was mostly used as a trigger. The others were used for the measurement of their mutual resolution and, in turn, the resolution of the S1. The signal from the S1 detector was preprocessed by a CFD (Constant Fraction Discriminator) unit to minimize its time-walk (with a threshold value of −400 mV). A custom software CFD was implemented in the offline analysis of raw signals from the photomultiplier to extract arrival times of generated pulses with respect to the trigger.

4. Measurements and results

There were three main goals: (1) the timing resolution of the detector using solid bars and comparisons to the glued counterparts, (2) the validation of the ToF model including modelling the MCP-PMT using analysis of raw signal waveforms, and (3) the timing resolution at a higher gain. The aim of the last goal was to compare the detector performance at gain levels used in the past ([7]). The last goal is mentioned in the Discussion section only because of its lower priority. Measurements were focused on the Train 2 which had been our reference train across all test measurements. Except the first train with a taper, other trains behave in a similar way. Mutual comparisons were investigated in the past [7]. During all measurements, the trigger S1 was positioned to have a coincidence with the following ToF areas in the beam: 0 mm from the edge (in short the edge), 5 mm, and 9 mm from the edge, see also Fig. 1(b). First, the timing resolution of the trigger (S1) was determined by means of a comparative timing resolution measurement among all SiPM detectors. The timing resolution of the trigger S1 detector was found to be 11 ± 1 ps. The photomultiplier #2199 was used for the main comparative measurements of glued and solid bars for three positions of the trigger. The #2200 was used for high gain studies. The different photomultipliers were compared in the framework of a configuration at 5 mm from the edge with solid bars and the normal operational gain (2000) of the PMTs.

4.1. Raw signal analysis

In this analysis, the focus was on the signal strength of glued and solid bars in the Train 2 as well as a comparison of bars within the train. This analysis was done in terms of the pulse area at the impedance load A_u^L and the number of photoelectrons N_{pe} which was calculated from the area using Eq. (2). After rearrangement and assuming the statistical behavior of the experimental data, the number of photoelectrons was estimated as follows:

$$\langle N_{pe} \rangle = -\frac{1}{e \cdot Z_L \cdot G_{SPE}} \langle A_u^L \rangle = -\frac{\eta}{e \cdot g \cdot Z_L \cdot G} \langle A_u \rangle = \frac{1}{g \cdot p} \langle A_u \rangle \tag{4}$$

where $\langle N_{pe} \rangle$ is a mean number of photoelectrons evaluated from a mean value of the pulse area $\langle A_u \rangle$ calculated from a set of events for the same conditions (number of events was 50 000 in our measurements); $g = 1000$ is the total gain of the preamplifiers; G is the (DC) gain of the photomultiplier; $\eta = 0.6$ is the collection efficiency; and the value of p is in Table 3.

Figure 9(a) shows a typical histogram of amplitudes for the solid Bar 2C with a good separation from the pedestal at −100 mV. Figure 9(b) demonstrates linearity between the amplitude and the area of the signal which is in turn proportional to the total charge (and the number of photoelectrons N_{pe}) generated within the photomultiplier. In this example, $k_s = 0.507$ ns.

Figure 10 shows the signal strength (signal areas at the load impedance) of the bars in the Train 2 for both the solid (in rich colors) and the glued (in pale colors) versions measured at

Optics EXPRESS

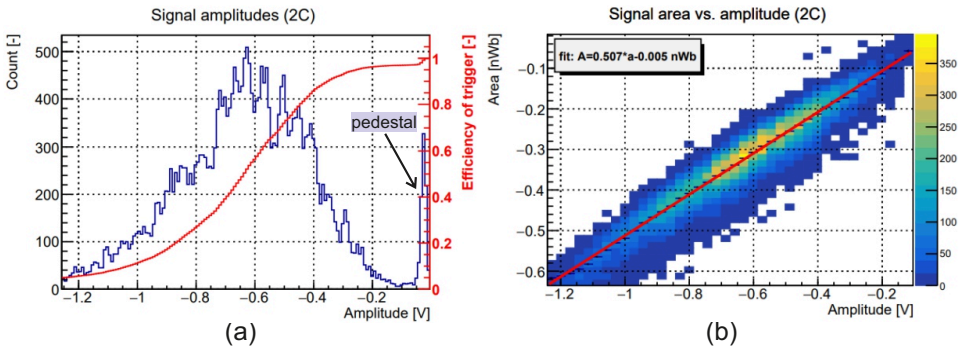

Fig. 9. Example of the raw signal analysis of the measurement of the solid Train 2 using the PMT #2199 at the DC gain of 2300 and the trigger position at 5 mm from the edge: (a) histogram of amplitudes taken from waveforms produced in the channel of the solid Bar 2C, (b) mutual dependency between the signal amplitude and its area (which is proportional to the total charge in pulse generated by the photomultiplier).

all specified distances from the edge of the bars (the trigger positions, see Fig. 1(b)). These values were obtained by dividing the measured signal areas by the amplification gain of 1000. The height of each box is equal to the span between quantiles 0.25 and 0.75 of the distribution of the areas given and the position of the black line in each box indicates its mean value. The corresponding ratios of pulse areas (solid bars vs. glued counterparts and among bars in the train) are summarized in Table 4. Here, S/G denotes the solid-to-glued ratio. The ratios 2B/2A, 2C/2A and 2D/2A are briefly denoted in summary as 2X/2A in the next text.

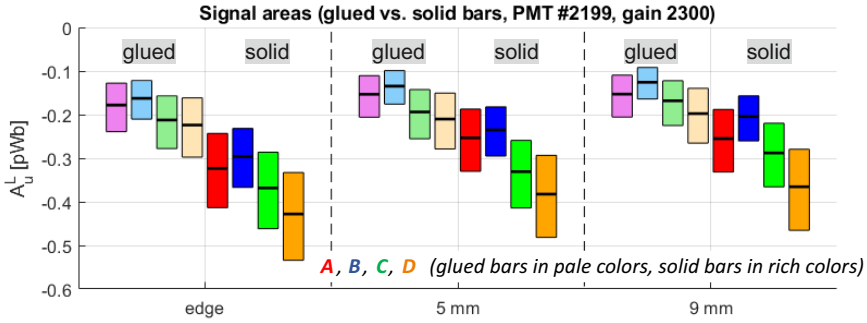

Fig. 10. Signal strength at the load impedance of bars in the Train 2 measured at various distance from the edge of the ToF for the (DC) gain of 2300 of the photomultiplier #2199.

On the one hand, the results revealed a discrepancy with regard to expectations in the case ratios between bars. The simulations predicted an augmentation of the signal in the channels 2B-2D compared to the first (upstream) Bar 2A by a factor of 1.2-1.7 based on the trigger position, see Table 1. Instead, the signal strength of the bar 2B was lower by approximately 10%. The Bars 2C and 2D produced stronger signals than the Bar 2A by a factor of 1.2-1.3 (at the edge) or 1.3-1.4 (5 mm and 9 mm) which was less than expected. This would mean that the channel of the Bar 2A has a higher amplification in the back-end side of the PMT electronics. On the other hand, S/G ratios are in an agreement with the simulations, see Fig. 11(a). This indicates the simulation satisfactorily predicted the number of photoelectrons generated in the deep UV region. See the Discussion section for a detailed analysis of this result.

Optics EXPRESS

Table 4. Measured mean pulse areas A_u^L in [pWb] of the bars in the Train 2 (solid and glued) using the PMT #2199. The parameter S/G stands for the ratio solid/glued of mean areas.

	Edge			5 mm			9 mm		
Bar	Glued	Solid	S/G	Glued	Solid	S/G	Glued	Solid	S/G
2A	−0.178	−0.323	1.8±0.7	−0.153	−0.256	1.7±0.7	−0.153	−255	1.7±0.7
2B	−0.163	−0.296	1.8±0.6	−0.135	−0.240	1.8±0.7	−0.126	−205	1.6±0.6
2C	−0.212	−0.368	1.7±0.6	−0.194	−0.331	1.7±0.6	−0.168	−288	1.7±0.7
2D	−0.224	−0.428	1.9±0.7	−0.210	−0.375	1.8±0.7	−0.198	−365	1.8±0.8
ratios									
2B/2A	0.9±0.4	0.9±0.3		0.9±0.4	0.9±0.3		0.8±0.3	0.8±0.3	
2C/2A	1.2±0.5	1.1±0.4		1.3±0.5	1.3±0.5		1.2±0.5	1.3±0.5	
2D/2A	1.3±0.5	1.3±0.5		1.4±0.6	1.5±0.5		1.2±0.5	1.4±0.5	

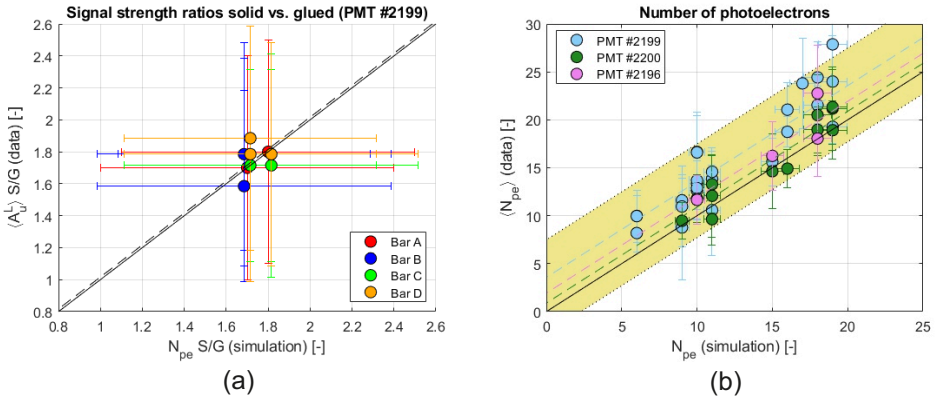

Fig. 11. Comparison of experimental data (CERN SPS, π^+, 120 GeV) with simulation for the Train 2: (a) ratios of pulse areas between solid bars and glued counterparts (Table 1) with corresponding ratios between the number of photoelectrons given by simulation (Table 4) using PMT #2199, (b) estimated number of photoelectrons. The yellow shaded area represents uncertainty of N_{pe} by data due to errors in determinations of the PMT gain, preamplifiers gain, and the impedance load. The solid black line denotes positions of the perfect match between data and simulation and the dashed lines indicate the mean shift of measured values from simulation results.

The plot in Fig. 11(b) summarizes how the simulation agrees with data in terms of an estimation of the number of photoelectrons generated and accepted by the photomultipliers according to Eq. (4). Each point represents a specific case of a bar type (A-D, solid or glued) and a trigger position. The solid black line denotes positions of the perfect match between data and simulation. For each photomultiplier, the dashed line represents a mean deviation from the simulation. The estimation of N_{pe} from data was affected with uncertainties in determination of the PMTs gains (±15%), fluctuations of the gain of preamplifiers across channels (±1 dB, ±10%), and the input impedance Z_i (±5%) of the PA-a preamplifiers (as noted earlier in the text). This uncertainty is a rather high ±6 p.e. and is visually depicted by the shaded yellow band in the figure. At first sight, the model slightly underestimates the number of photoelectrons compared to data by 2.6 p.e. on average.

Optics EXPRESS

4.2. Timing performance

Timing resolution is the main characteristics of the ToF detector. By design, a crossing particle hits one of four trains triggering (possibly) all bars in the train. Thus, the resolution is given by timing resolutions of the individual trains. The timing resolution of a train was calculated as an amplitude-weighted average of arrival times measured in each bar of the train. This weighted sum approach gives a higher importance to those signal outputs with higher amplitudes in the average. It could happen that only three or two bars or even one bar triggers. The timing resolution is affected correspondingly. The timing performance was analyzed for all trigger cases in which all bars or at least given number of bars triggered. It showed that all four bars triggered together in most cases (94%). Thus in the following, only the case was considered in which all four bars in a train triggered.

Figure 12(a) shows results from the analysis of the timing resolution of the glued and the solid bars. For each trigger position, solid bars exhibited a better resolution by 4 ps on average. The timing resolution of the whole solid Train 2 improved as well by 3 ps on average. Its resolution was: 20 ± 2 ps at the edge, 22 ± 2 ps at 5 mm, and 24 ± 2 ps at 9 mm from the edge. Figure 12(b) summarizes these results for solid bars only with all photomultipliers in various trigger positions. As expected, there were no significant differences in the timing resolution among the photomultipliers. There is a worse timing resolution of the PMT #2196 at the channel of the Bar 2A which could be attributed to the lower strength of the signal output at this channel (probably due to a worse response of the PMT pixel). The timing resolution of the full Train 2 at 5 mm was: 24 ± 2 ps for the #2196, 23 ± 2 ps for the #2199, and 21 ± 2 ps for the #2200. At the edge, the timing resolution for the setup with the PMTs #2199 and the #2200 was 20 ± 2 ps and 19 ± 2 ps respectively. The only #2199 was used or measurements at 9 mm from the edge giving 24 ± 2 ps.

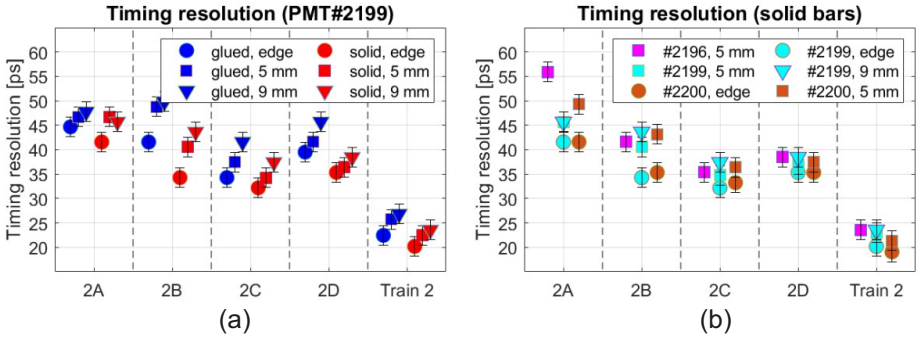

Fig. 12. Results of timing resolution measurements: (a) comparison of glued and solid bars of the Train 2 using the PMT #2199, (b) results for solid bars and all photomultipliers. Photomultipliers were operated at 1545V (HV divider ratio 1:10:1) providing the gain 1800 (#2196), 2300 (#2199), or 2100 (#2200).

5. Discussion

The timing performance is the main characteristics of the ToF detector. Its recent upgrade addressed all shortcomings of the original ToF version while maintaining its proven radiation hardness which is critical in conditions of the LHC environment (total expected dose of 400 kGy/year at a distance of 5 mm from the beam centre). There were worried that changes in its construction (the additional separation window) and its low PMT operational gain (down to 2000) would significantly deteriorate the timing resolution. Values measured in the vicinity of 20 ps are acceptable for the AFP project. The PMTs #2200 and #2199 particularly gave promising

Optics EXPRESS

results. Based on the results of rate measurements [10], both devices were chosen for installation in the LHC environment.

Solid bars helped a lot to maintain the timing resolution at around 20 ps. All the mentioned results of the timing resolution were valid for low rates of passing particles per train (tens of kHz). In the LHC, the rate will be 20 MHz per train. In general, the performance of photomultipliers decreases at these rates due to limits in the speed of charge replenishing of the MCP. This causes a drop of its actual (effective) gain [10,11]. As mentioned in the Introduction, laser measurements showed that there was no gain drop of the PMT #2199 and #2200 at 20 MHz and at the gain of 2000. Thus, these two PMTs should operate with the same performance in the LHC tunnel at that gain. The arrival time of a whole train was calculated as a (weighted) arithmetic average of the arrival time of each bar. Looking at Fig. 12, the mean resolution of each bar in the Train 2 was roughly $\sigma_b = 38$ ps (across all the PMTs, trigger at 5 mm from the edge). This theoretically corresponds to the train resolution $\sigma_t = 19$ ps applying the rule $\sigma_t = \sigma_b/\sqrt{N}$, where $N = 4$ is number of bars in the train. This rule is valid if there is no crosstalk among the bars. The mean measured timing resolution of the Train 2 was about 21 ps, close to $\widetilde{\sigma_t}$. This indicates that the crosstalk was small which was one of the goals of the suggested changes in the backend electronics of the photomultipliers.

It is common that pixels behave non-uniformly across a MCP-PMT due to space inhomogeneities both of the photocathode QE and the emissive layer in the MCP as well as due to amplification variations of the amplifiers across channels (approximately ±10%). Thus, there is no reason to compare the experimental data with the simulation in terms of pulse area ratios among bars in train (like 2X/2A in Table 4). Comparisons between solid and glued bar counterparts are however not affected by this issue. As seen in Fig. 11(a), there is a good agreement between the simulation and the experimental data in this way. One drawback of the simulation was the unknown quantum efficiency of the MCP-PMT photocathode at wavelengths below 200 nm (in deep UV). We simply assigned the value of 0.16 at the lowest known wavelength of 200 nm to the region down to 160 nm. By nature, the production of Cherenkov photons grows rapidly with lower wavelengths and any significant changes of QE below 200 nm would cause a serious deviation of the real response from that of the model. An analysis of the S/G ratios (Fig. 11(a)) indicates the simulation satisfactorily predicted the number of photoelectrons generated in the deep UV region when taking into consideration that the glued bars effectively work down to 233 nm due to the glue cut-off point and solid bars work down to 160 nm [9]. Thus, the QE is around 0.16 on average below 200 nm.

Measurements at high gains ($10^4 - 10^5$) with the PMT #2200 during the beam test measurements were performed to see what timing resolution we could expect at normal operational gains. We reached a timing resolution of down to 15 ps at the DC gain of $3.5 \cdot 10^4$ and at the edge which is comparable with our results in the past with the simpler geometry of the ToF [6,7]. However, the conditions at the LHC don't allow the ToF operation at those gain levels without a significant loss of efficiency.

We also tried to predict the output signal strength from the photomultipliers by means of an equivalent electrical circuit, see Fig. 5. The credibility of such a model depends both on its complexity and a correct estimation of each component, in particular parasitic impedances. The model was successfully verified in the past on data from laser measurements comparing amplitudes on one-photoelectron levels at the light wavelength of 405 nm. The comparison with beam test data presented here was more difficult due to its higher complexity - especially the wide spectral range of incoming Cherenkov light (from 160 nm to 600 nm) associated with a spread distribution of photoelectrons in time, and the complex geometry of the optical part.

Optics EXPRESS

6. Conclusion

Last two years, the ToF detector for the AFP project underwent significant design changes to remove various construction shortcomings. The throughput of its optical system was affected by the extra quartz window in the light path. Beside this, there was the requirement of operating the photomultiplier at lower gains close to 2000 to compensate for the signal attenuation at high pulse rates of 20 MHz. A new backend electronics of MCP-PMTs was designed in cooperation with Photonis, Inc. to suppress the electronic crosstalk among channels, to adapt to our changes in the ToF design, and to improve protection against external electromagnetic interference.

Based on these modifications, Photonis produced four new ALD coated miniPlanacon XPM85112-S-R2D2 photomultipliers for us: S/N 9002196 (MCP resistance of 44 MΩ), 9002199 (35 MΩ), 9002200 (27 MΩ), and 9002201 (55 MΩ). We proposed their equivalent electrical model. We used it also to extend our simulations of the ToF detector by calculations of the output signal waveforms based on simulated time distributions of the initial Cherenkov pulse done in Geant4. The beam test measurements at the CERN SPS beam proved the credibility of such a model, although improvements are still needed. Namely, a model of QE in deep UV region must be better specified (need to measure). There is also a plan to measure irradiated bars from the LHC environment in the SPS beamtest facility to better understand the effect of the radiation damage.

The measurements confirmed the detector kept its timing resolution of 20 ps at low gain levels of its photomultiplier (order of 10^3). Without gain constrains, we reached the limit of 15 ps at a gain of $3.5 \cdot 10^4$. The detector is now installed in the LHC tunnel and is ready for running in the Run 3 campaign of the LHC.

Funding. Narodowe Centrum Nauki (UMO-2019/34/E/ST2/00393); Ministerstwo Edukacji i Nauki (2022/WK/08); Ministarstvo Prosvete, Nauke i Tehnološkog Razvoja (451-03-68/2022-14/200105); Univerzita Palackého v Olomouci (IGA_PrF_2022_004); European Regional Development Fund (CZ.02.1.01/0.0/0.0/16_019/0000754); Ministerstvo Školství, Mládeže a Tělovýchovy (LM2018104, LTT 17018).

Acknowledgments. The measurements leading to these results have been performed at the H6 beamline of the SPS North Area at CERN.

Disclosures. The authors declare no conflicts of interest.

Data availability. Data underlying the results presented in this paper are not publicly available at this time but may be obtained from the authors upon reasonable request.

References

1. A. B. Kaidalov, V. A. Khoze, A. D. Martin, and M. G. Ryskin, "Extending the study of the higgs sector at the lhc by proton tagging," Eur. Phys. J. C **33**(2), 261–271 (2004).
2. FP420 Collaboration, "The FP420 R&D project: Higgs and New Physics with forward protons at the LHC," J. Instrum. **4**(10), T10001 (2009).
3. L. Adamczyk, E. Banas, A. Brandt, M. Bruschi, S. Grinstein, J. Lange, M. Rijssenbeek, P. Sicho, R. Staszewski, T. Sykora, M. Trzebinski, J. Chwastowski, and K. Korcyl, "Technical Design Report for the ATLAS Forward Proton Detector," (2015). Technical Report CERN-LHCC-2015-009. ATLAS-TDR-024.
4. K. Cerny, T. Sykora, M. Tasevsky, and R. Zlebcik, "Performance studies of Time-of-Flight detectors at LHC," J. Instrum. **16**(01), P01030 (2021).
5. L. Nozka, A. Brandt, M. Rijssenbeek, T. Sykora, T. Hoffman, J. Griffiths, J. Steffens, P. Hamal, L. Chytka, and M. Hrabovsky, "Design of cherenkov bars for the optical part of the time-of-flight detector in geant4," Opt. Express **22**(23), 28984–28996 (2014).
6. L. Nozka, L. Adamczyk, G. Avoni, A. Brandt, P. Buglewicz, E. Cavallaro, G. Chiodini, L. Chytka, K. Ciesla, P. M. Davis, M. Dyndal, S. Grinstein, P. Hamal, M. Hrabovsky, K. Janas, K. Jirakova, M. Kocian, T. Komarek, K. Korcyl, J. Lange, D. Mandat, V. Michalek, I. L. Paz, D. Northacker, M. Rijssenbeek, L. Seabra, P. Schovanek, R. Staszewski, P. Swierska, and T. Sykora, "Construction of the optical part of a time-of-flight detector prototype for the AFP detector," Opt. Express **24**(24), 27951–27960 (2016).
7. L. Chytka, G. Avoni, A. Brandt, E. Cavallaro, P. M. Davis, F. Foerster, M. Hrabovsky, Y. Huang, K. Jirakova, M. Kocian, T. Komarek, K. Korcyl, J. Lange, V. Michalek, L. Nozka, I. L. Paz, M. Rijssenbeek, P. Schovanek, T. Sykora, and V. Urbasek, "Timing resolution studies of the optical part of the AFP time-of-flight detector," Opt. Express **26**(7), 8028–8039 (2018).

Optics EXPRESS

8. J. Lange, E. Cavallaro, S. Grinstein, and I. L. Paz, "3D silicon pixel detectors for the ATLAS Forward Physics experiment," J. Instrum. **10**(03), C03031 (2015).
9. L. Nozka, A. Brandt, K. Cerny, M. Hrabovsky, T. Komarek, F. Krizek, D. Mandat, M. Milovanovic, M. Rijssenbeek, P. Schovanek, T. Sykora, V. Urbášek, and J. Zatloukal, "Performance studies of new optics for the time-of-flight detector of the AFP project," Opt. Express **28**(13), 19783–19796 (2020).
10. T. Komarek, V. Urbasek, A. Brandt, K. Cerny, J. DeFazio, V. Georgiev, M. Hrabovsky, Z. Kubik, L. Nozka, D. Orlov, S. D. Pinto, M. Rijssebeek, T. Sykora, and J. Zich, "Characterization of the miniPlanacon XPM85112-S-R2D2 MCP-PMT with a custom modified backend electronics," Nucl. Instrum. Methods Phys. Res., Sect. A **1041**, 167330 (2022).
11. T. Komarek, A. Brandt, V. Chirayath, L. Chytka, M. Hrabovsky, L. Nozka, M. Rijssenbeek, T. Sykora, and V. Urbasek, "Timing resolution and rate capability of Photonis miniPlanacon XPM85212/A1-S MCP-PMT," Nucl. Instrum. Methods Phys. Res., Sect. A **985**, 164705 (2021).
12. D. Orlov, T. Ruardij, S. D. Pinto, R. Glazenborg, and E. Kernen, "High collection efficiency MCPs for photon counting detectors," J. Instrum. **13**(01), C01047 (2018).
13. Geant4 Collaboration, "Recent developments in Geant4," Nucl. Instrum. Methods Phys. Res., Sect. A **835**, 186–225 (2016).
14. P. M. Duarte, "Quartic: An ultra-fast time-of-flight counter," Ph.D. thesis, The University of Texas, Arlington (2007).
15. G. Brocard, "The LTspice IV Simulator: Manual, Methods and Applications," Swiridoff Verlag, Wurth (2013).
16. F. Tang, "Modeling for MCP-PMT Output Signal," presentation in frame of LAPPD project (2008).
17. J. Lange, L. Adamczyk, G. Avoni, E. Banas, A. Brandt, M. Bruschi, P. Buglewicz, E. Cavallaro, D. Caforio, G. Chiodini, L. Chytka, K. Ciesla, P. M. Davis, M. Dyndal, S. Grinstein, K. Janas, K. Jirakova, M. Kocian, K. Korcyl, I. L. Paz, D. Northacker, L. Nozka, M. Rijssenbeek, L. Seabra, R. Staszewski, P. Swierska, and T. Sykora, "Beam tests of an integrated prototype of the ATLAS forward proton detector," J. Instrum. **11**(09), P09005 (2016).
18. M. Albrow, H. Kim, S. Los, M. Mazzillo, E. Ramberg, A. Ronzhin, V. Samoylenko, H. Wenzel, and A. Zatserklyaniy, "Quartz Cherenkov Counters for Fast Timing: QUARTIC," J. Instrum. **7**(10), P10027 (2012).
19. L. Chytka, M. Hrabovsky, T. Komarek, V. Michalek, L. Nozka, T. Sykora, and V. Urbasek, "Time resolution of the SiPM-NUV3S," Nucl. Instrum. Methods Phys. Res., Sect. A **935**, 51–55 (2019).
20. M. Bonesini, T. Cervi, A. Menegolli, M. C. Prata, G. L. Raselli, M. Rossella, M. N. Spanu, and M. Torti, "Detection of vacuum ultraviolet light by means of SiPM for high energy physics experiments," Nucl. Instrum. Methods Phys. Res., Sect. A **912**, 235–237 (2018).